Regulating the trap distribution of $ZnGa_2O_4:Cr^{3+}$ by Li^+/Ga^{3+} doping for upconversion-like trap energy transfer NIR persistent luminescence

Junqing Xiahou[1], Qi Zhu[1*], Fan Li[1], Minghui Jin[1], Lin Zhu[2], Sai Huang[1], Tao Zhang[3], Xudong Sun[4], and Ji-Guang Li[5*]

[1]*Key Laboratory for Anisotropy and Texture of Materials (Ministry of Education), School of Materials Science and Engineering, Northeastern University, Shenyang, Liaoning 110819, PR China*

[2]*College of Sciences, Northeastern University, Shenyang Liaoning 110819, PR China*

[3]*Shenyang National Laboratory for Materials Science, Northeastern University, 3-11 Wenhua Road, Shenyang, Liaoning 110819, PR China*

[4]*Foshan Graduate School of Northeastern University, Foshan, Guangdong 528311, PR China*

[5]*Research Center for Functional Materials, National Institute for Materials Science, Namiki 1-1, Tsukuba, Ibaraki 305-0044, Japan*

[*]Corresponding author:

Dr. Qi Zhu

Tel: +86-24-8367-2700

E-mail: zhuq@smm.neu.edu.cn

Dr. Ji-Guang Li

Tel:+81-29-860-4394

E-mail: LI.Jiguang@nims.go.jp

Abstract

$ZnGa_2O_4:Cr^{3+}$ persistent luminescent phosphors (PLPs) have been widely applied in bioimaging and photonics due to their ultra-long near-infrared (NIR) afterglow. However, UV and visible excitation currently in use have shallow penetration depth or harmful effect on organism, which limits the long-term bioimaging. Therefore, developing NIR PLPs excited by NIR light is urgent for bioimaging. Here, $Zn_{1-x}(Li/Ga)_xGa_2O_4:Cr^{3+}$ (x=0-1) NIR PLPs were synthesized. All the newly introduced Ga^{3+} ions occupy the tetrahedral sites. However, with increasing Li^+/Ga^{3+} content, Li^+ ions firstly occupy the tetrahedral position, then partially enter octahedral sites, and completely occupy the octahedral sites at x=1. Incorporation of Li^+/Ga^{3+} contributes to the weakened crystal field strength, which leads to a deeper trap depth and a wider trap energy level. A complete replacement of Zn^{2+} by Li^+/Ga^{3+} ions leads to the splitting of the trap energy level into two-divided ones, which reduces the electron transfer between deep/shallow traps and makes the deep trap energy level be near to the ^2E energy level of Cr^{3+}. Therefore, an enhanced NIR afterglow excited by the low-energy NIR light is found for the Li^+/Ga^{3+} doped sample. This work provides a new category for the NIR-absorptive-NIR-emissive PLPs and proposes a new application for long-term bioimaging.

Keywords: near-infrared persistent luminescence; crystal field strength; trap depth; low-energy excitation

1. Introduction

In recent decades, near-infrared (NIR) persistent luminescent phosphors (PLPs) have shown broad application prospects in the field of biological imaging mainly due to their two advantages: (1) The avoidance of self-fluorescence from biological tissue due to excitation in vitro; (2) The high spatial resolution, deep penetration depth, and low optical absorption of NIR optical signals through the organism. Trivalent chromium ion (Cr^{3+}) is a near-infrared red doping ion because of its emission range from 650 to 1600 nm.[1-3] Based on the above reasons, spinel long persistent luminescence materials of Cr^{3+}-doped $ZnGa_2O_4$, $Zn_3Ga_2Ge_2O_{10}$, and other similar gallate hosts have become the research hotspots in the field of luminescence and biological imaging due to their near-infrared emission and long afterglow characteristics.[4-6] Subsequently, a variety of functionalized zinc gallates or zinc gallogermanates nanoparticles with NIR long afterglow were applied in biological imaging, life sciences, and biomedicine.[7-9]

The research on the spinel-structure NIR persistent luminescence materials mainly focuses on two aspects: 1. Using monodisperse luminescent particles as the fluorescent probes for different biological applications, including live animal imaging, drug delivery, tumor imaging, etc. 2. Regulating the crystal structure for improved persistent luminescence, such as co-doping $Cr^{3+}/Ge^{4+}/Sn^{4+}$, $Cr^{3+}/Mg^{2+}/Ge^{4+}$, $Cr^{3+}/Zn^{2+}/Sn^{4+}$, Cr^{3+}/Li^{+}, Cr^{3+}/Pr^{3+}, $Cr^{3+}/Al^{3+}/Bi^{3+}$, and $Cr^{3+}/Gd^{3+}/Sn^{4+}$ in zinc gallate.[10-16] $ZnGa_2O_4:Cr^{3+}$ belongs to cubic spinel structure, which contains 56 atoms in the *F*-$d\bar{3}$m. In $ZnGa_2O_4$, Zn^{2+} ions occupy the 8a sites (CN=4, CN: coordination number), Ga^{3+} ions occupy the 16d sites (CN=6).[2, 10, 11, 17] For $ZnGa_2O_4:Cr^{3+}$, Cr^{3+} would like to replace Ga^{3+} in octahedron site, because Cr^{3+} and Ga^{3+} ions have similar ionic radii (R_{Cr}=0.63 Å; R_{Ga}=0.62 Å) in octahedron.

Cr^{3+} ions are doped in spinel-structured gallates as the emitters, and the crystal field as well as defect regulation are crucial for the improvement of photoluminescence and persistent luminescence. The optical absorption and luminescence of the Cr^{3+} ions can be remarkably influenced by host materials because the energy levels of the d

electrons of Cr^{3+} ions are dependent on the symmetry of oxygen coordination and crystal field strength.[3, 18, 19] Cr^{3+} ions can emit a broadband emission at ~650-1600 nm (the spin-allowed $^4T_2 \rightarrow {}^4A_2$ transition) and a narrow-band emission at ~700 nm (the spin forbidden $^2E \rightarrow {}^4A_2$ transition) in a weak and strong crystal field, respectively. However, the ^2E and $^4T_2$ levels are overlapped in the intermediate crystal field, leading to coincidence of these two transitions from $^4T_2/^2E$ to $^4A_2$. Recently, the investigations on the influence of crystal field on luminescence by co-doping different ions have been widely reported. However, investigations about the effect of crystal field on the electron traps and the persistent luminescence are rather limited.

The afterglow behavior has been attributed to the Cr^{3+} ion and nearby anti-site defect interactions in the spinel $ZnGa_2O_4$ based on the currently accepted model. Research showed that traps play an important role as active centers in persistent phosphors of $ZnGa_2O_4:Cr^{3+}$. Changing the Zn ratio or incorporating other metal cations is the effective ways to change the trap distribution and depth of phosphors, and further improve their persistent luminescence. However, the exact effect of the trap depths and distributions on persistent luminescence have not been defined.[14, 20-22] On one hand, the slowly released electrons from the deep traps influence the afterglow of persistent phosphor, and the deeper traps result in the slower release of electrons from traps, which contributes to a longer afterglow;[22-24] On the other hand, higher density and larger number of traps may contribute to a stronger afterglow.[22, 25] Moreover, some studies indicate that the trap distribution also affects the light storage of various energies or various wavelengths.[19, 26, 27] In general, low-energy excitation can not excite the electrons to the traps. However, continuously distributed traps result in up-convertible-like trap energy storage and electron transfer between deep traps (DTs) and shallow traps (STs), which facilitates biological imaging of in situ long-wavelength excitations.[26] However, deep traps and shallow traps are continuously distributed for most materials, which leads to rapid energy transfer between traps and accelerates the release of electrons from deep traps. Therefore, the reconstruction and segmentation of trap distribution may regulate the electron transfer between DTs and STs and thus improve the near-infrared persistent luminescence of phosphors.

Herein, a series of $Zn_{1-x}(Li/Ga)_xGa_2O_4:Cr^{3+}$ (x=0-1) NIR PLPs were synthesized using a solid-state reaction. As Li^+/Ga^{3+} content increases, the crystal field strength of phosphors decreases, which makes a redshift of excitation and emission spectra. The crystal field also affects the trap depth and distribution. A complete replacement of Zn^{2+} by Li^+/Ga^{3+} ions leads to the splitting of the trap energy level, which reduces the electron transfer between DTs and STs, but enhances the NIR afterglow by low-energy excitation. The outcome in this work provides a new category for the persistent luminescence nanoparticles with a NIR-absorptive-NIR-emissive feature and a new application for biological imaging.

2. Experimental section

All the experimental methods are described in detail in supporting information.

3. Results and discussion

3.1 Synthesis and local structure of $Zn_{1-x}(Li/Ga)_xGa_2O_4:0.005Cr^{3+}$

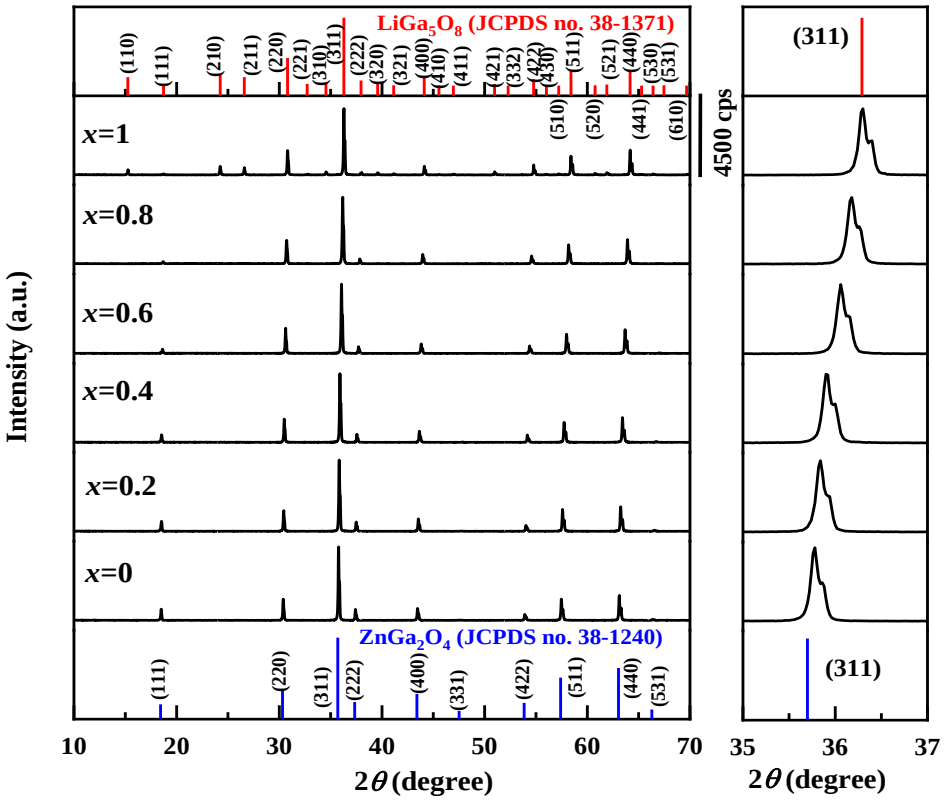

Figure 1. XRD patterns for $Zn_{1-x}(Li/Ga)_xGa_2O_4:0.005Cr^{3+}$ (x=0-1) calcined at 1300 ^oC.

A series of $Zn_{1-x}(Li/Ga)_xGa_2O_4$:0.005Cr^{3+} (x=0-1) powders were synthesized and the XRD were performed to analyze the crystal structure and phase transition in Figure 1. The measured XRD patterns of x=0-0.8 indicate a crystalline structure corresponding to the reference pattern for $ZnGa_2O_4$ (ZGO) of spinel structure (JCPDS File No. 38-1240). However, $LiGa_5O_8$ (LGO) cubic phase (JCPDS File No. 38-1371) with new diffraction peaks appears only at the larger x value of 1. The reference patterns of $LiGa_5O_8$ (JCPDS File No. 38-1371) correspond to a spinel structure with the space group of $P4_332$, a derivative of the $Fd\bar{3}m$ space group of spinel structure. Furthermore, the (311) main diffraction of spinel gradually shifts to the bigger angle side with increasing the x value, and the lattice constant of the powders decreases from a=8.338 to 8.203 Å with the value of x increasing from 0 to 1 (Table S1), indicating that the unit cell is shrink by substitution of Zn^{2+} with the Li^+/Ga^{3+} pair. For convenient description, $Zn_{1-x}(Li/Ga)_xGa_2O_4$:0.005Cr^{3+} and $Zn_{1-x}(Li/Ga)_xGa_2O_4$ are denoted as ZLGGC and ZLGGO hereafter.

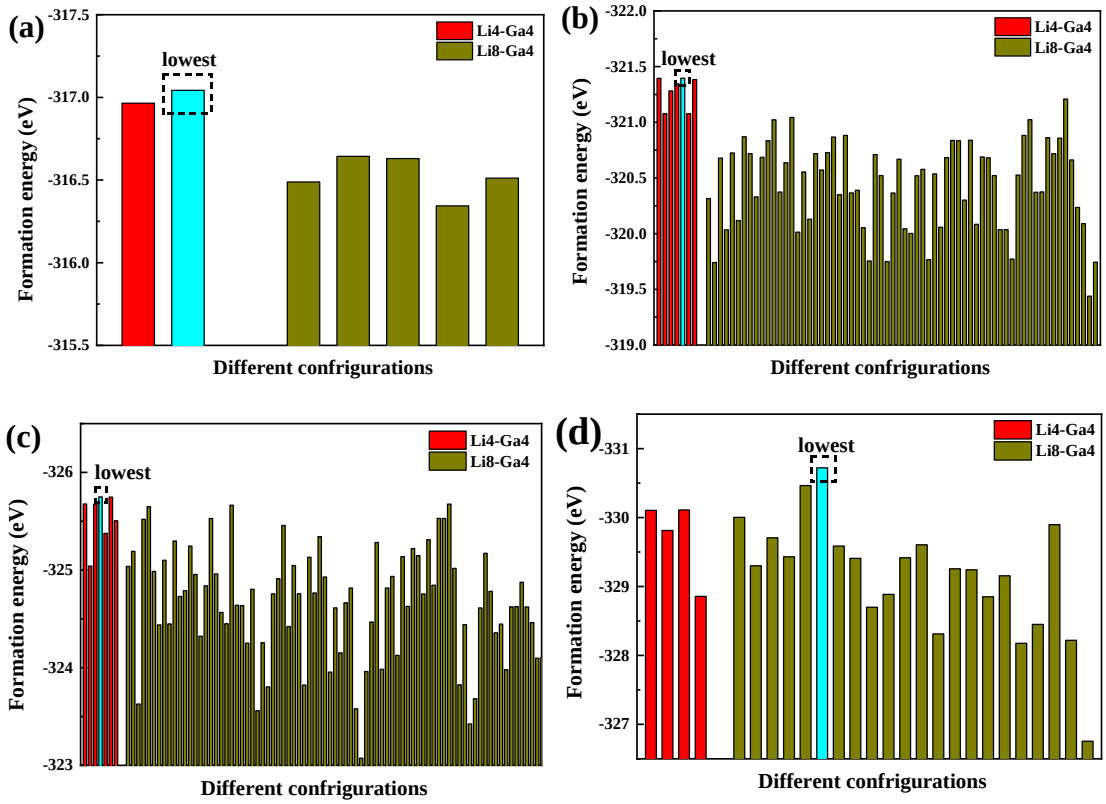

Figure 2. The DFT total energy of the unit cell with different doping contents of Li/Ga: (a) 25%, (b) 50%, (c) 75%, (d) 100%.

Table 1. The calculated energy difference (ΔE_d) with various Li/Ga doping content.

Li/Ga content	E(Li4-Ga4) (eV)	E(Li8-Ga4) (eV)	ΔE_f (eV)
25%	-317.043	-316.643	0.4
50%	-321.396	-321.209	0.187
75%	-325.750	-325.676	0.074
100%	-330.109	-330.721	-0.612

It is known that, in the structure of ZGO spinel, Ga^{3+} ions occupy the 16d sites, Zn^{2+} ions occupy the 8a sites, with O occupying the 32e sites. In this work, co-substitution of Li^+/Ga^{3+} for Zn^{2+} results in a smaller lattice constant. A complete replacement of Zn^{2+} by Li^+/Ga^{3+} ions leads to the LGO spinel structure: The Ga^{3+} ions occupy both the 8c (CN = 4) and 12d sites (CN = 6), and the Li^+ ions occupy only the 4b sites (CN = 6). Four oxygens are surrounding the tetrahedral site, and six oxygens surround the octahedral site.[17, 28, 29] It is noticed that Li^+, Zn^{2+}, and Ga^{3+} ions have different radii in different coordination environments: Li^+ (r^{IV} = 0.59 Å, r^{VI} = 0.67 Å), Zn^{2+} (r^{IV} = 0.60 Å, r^{VI} = 0.74 Å), and Ga^{3+} (r^{IV} = 0.47 Å, r^{VI} = 0.62 Å). Referring to the ionic radius, Li^+/Ga^{3+} ions prefer occupying Zn^{2+} sites, but the specific occupations need to be determined by a variety of structural detection.[11, 22, 30]

Different configurations were built for formation energy calculation to explore the site preference of Li^+/Ga^{3+} doping in $ZnGa_2O_4$. There are two conditions for Li/Ga doping in spinel $ZnGa_2O_4$: (1) Li and Ga occupy the tetrahedral sites; (2) Li occupies the octahedral sites and Ga occupies the tetrahedral sites, which are defined as Li4-Ga4 and Li8-Ga4, respectively. Figure 2 demonstrates the unit cell's density functional theory (DFT) total energy with different Li/Ga content doping. As shown in Figure 2, two, seven, seven, and four crystal structure models are created for the tetrahedral positions occupied by Li and Ga (Li4-Ga4) with 25%, 50%, 75%, and 100% Li/Ga content, respectively. There are 5, 66, 106, and 22 crystal structure models created for calculating the DFT total energy of Li in the octahedron and Ga in the tetrahedron (Li4-Ga8) with 25%, 50%, 75%, and 100% Li/Ga content, respectively. The energy difference (ΔE_d) of conditions for Li/Ga doping was calculated as follows:[22, 31, 32]

$$\Delta E_d = E(\text{Li4-Ga4}) - E(\text{Li8-Ga4}) \quad (1)$$

where *E*(Li4-Ga4) is the unit cell's lowest DFT total energy with Li and Ga occupying the tetrahedral sites, *E*(Li8-Ga4) is the unit cell's lowest DFT total energy with Li in the octahedron and Ga in the tetrahedron. All the calculated results are demonstrated in Table 1. When the content of Li^{+}/Ga^{3+} is not more than 75%, the energy difference is calculated as 0.4 (25%), 0.187 (50%), and 0.074 (75%) eV, which indicates that the most likely placeholder in ZLGGO is Li and Ga both in tetrahedral sites. However, the energy difference decreases with increasing Li/Ga content. When the Li/Ga content reaches 100%, the energy difference was calculated to be -0.612 eV, which indicates that the most likely placeholder in the x=1 sample is Li in octahedral and Ga both in octahedral and tetrahedral sites. According to the calculation results, the lowest energy configurations with different contents of Li/Ga doped in spinel $ZnGa_2O_4$ are shown in Figure 3.

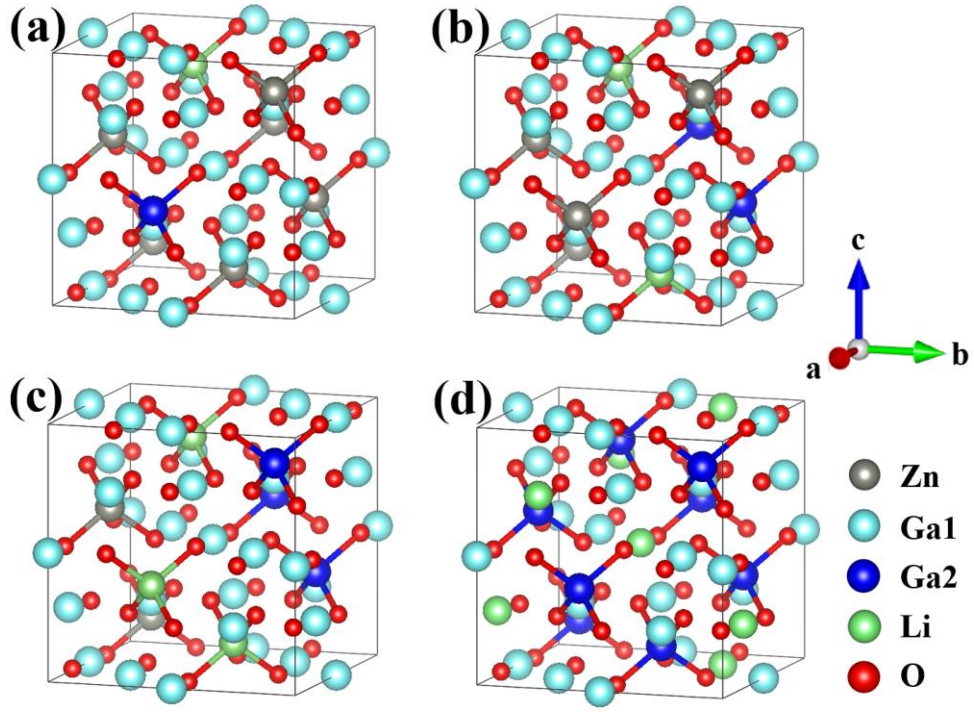

Figure 3. 56-atom unit cells crystal structure with different contents of Li/Ga doped in spinel $ZnGa_2O_4$ at condition of the lowest energy: (a) 25%, (b) 50%, (c) 75%, (d) 100%.

To explore the occupations of Li^{+} and Ga^{3+} ions in tetrahedral and octahedral sites, the ^{7}Li and ^{71}Ga solid-state MAS NMR spectra of ZLGGO powder were obtained (Figure S1 and Figure 4a). With increasing Li^{+}/Ga^{3+} concentration, the peaks in ^{7}Li

NMR spectra move to the high chemical shift, which means the Li^+ ions move from tetrahedron to octahedron. There are interactions between electric field gradients and nucleus quadrupolar moment for ^{71}Ga, a half-integer quadrupolar nucleus (I=3/2), which leads to the NMR spectra to be correspondingly broadened.[10, 33] Fast sample spinning frequencies and high magnetic fields are required for the resolution of the corresponding resonances in MAS spectra. [10] The coordination numbers and local symmetries significantly influence the shifts of ^{71}Ga MAS NMR line of the central transition.[33, 34] The range of Ga in an octahedral or tetrahedral environment will be 80 to 42 ppm, and 107 to 222 ppm, respectively.[10, 34-36] Solid nuclear magnetic field-tested at high speed will produce rotating sidebands, which is the peak caused by the rotor rotating at high speed in the probe. The sideband peaks are easy to be identified because they are symmetric relative to the main peak, and the distance from sideband peak to main peak is the frequency of rotation. As shown in Figure 4a, the peak of Ga^{IV} overlaps with the sideband, which makes it difficult to directly quantify the content of Ga in octahedron. The peak integral area ratio in NMR spectra is used to quantitatively analyze the content of Ga^{3+} in tetrahedron and octahedron. The areas of ~-110-~15 ppm, ~15-~90 ppm, and ~90-~230 ppm are defined as Regin1 (R1), Regin2 (R2), and Regin3 (R3), respectively. The quantification of Ga^{IV}/Ga^{VI} proportion can be determined from the three areas of signal integration using the following formula: (R3-R1)/R2 (Figure S2). As shown in Table 2, the quantification of Ga^{IV}/Ga^{VI} in ZGO determined from ^{71}Ga NMR spectra were of ~1.7%, ~5%, ~21%, and ~66% for the x = 0, 0.2, 0.6, and 1 samples, respectively. The Ga^{IV}/Ga^{VI} ratios of x=0 and x=1 samples are 1.7% and 66%, which agree with the spinel inversion in ZGO and the sites allocation in LGO reported in previous results.[10, 11, 28, 36] The Ga^{IV}/Ga^{VI} ratio of ZLGGO measured from the MAS NMR spectrum increases from 1.7% to 66% with the Li^+/Ga^{3+} content increases from 0 to 100%. This indicates that more Ga^{3+} ions and Li^+ ions occupy the tetrahedron and octahedron respectively at a higher x value.

Raman spectroscopy was performed to further reveal the changes for structure in Figure 4b. Cubic spinel contains 42 vibrational modes in its group theory. The

following modes of spinels are predicted by group theory analysis at the Γ point:[18, 37-40]

$$\Gamma=A_{1g}(R)+E_g(R)+T_{1g}+3T_{2g}(R)+2A_{2u}+2E_u+4T_{1u}(IR)+ T_{1u}+2T_{2u} \quad (2)$$

where most modes are silent or acoustic modes except the indicated infrared-active and Raman-active modes. There are only four infrared active modes and five Raman active modes in normal non-defective spinels. In general, the mode frequencies follow the sequence: $T_{2g}<E_g<T_{2g}<T_{2g}<A_{1g}$.The spinel $ZnGa_2O_4$ first-order Raman active mode is due to the tetrahedral site Zn^{2+} ions, but has nothing to do with the octahedral site cations, suggesting ZnO_4 group is the only contributor to the first-order Raman mode. In AB_2O_4, the highest frequency T_{2g} Raman-active mode is assigned to the AO_4 tetrahedron symmetric stretching vibration, the remaining T_{2g} mode is assigned to the BO_6 octahedron translation against the A cation, and the E_g and A_{1g} Raman-active modes correspond to the symmetric bending motion of the AO_4 unit oxygens and the asymmetric bending motion of the A bonded oxygens, respectively.[37] For x=0 sample, the Raman spectra peak at ~453, ~609, and ~713 cm^{-1}, corresponding to T_{2g}, T_{2g}, and A_{1g} modes (k=0), respectively. The number of Raman-active modes is related to the material's crystal symmetry. When the crystal transforms to a lower symmetry, splitting of degenerate vibration modes or a new Raman mode can be seen. The peaks at ~713 and ~609 cm^{-1} correspond to the asymmetric bending motion of the Zn bonded oxygens in $ZnGa_2O_4$ and the symmetric stretching vibration of the ZnO_4 tetrahedron, respectively (Figure 4b). They gradually weaken and then disappear with increasing the Li^+/Ga^{3+} concentration. Incorporating Li^+/Ga^{3+} in the lattice reduces the intensity of Raman bands, hinting at the onset of disorder of cations among the octahedral and tetrahedral sites. Meanwhile, Li^+/Ga^{3+} doping leads to splitting of T_{2g} and A_{1g} vibration modes at ~648 and ~734 cm^{-1}, indicating that the structure transforms into a lower symmetry. Due to the low-frequency Raman-active mode of T_{2g} is the GaO_6 octahedron against the incorporation of Li^+ cations, it becomes stronger with increasing the Li^+/Ga^{3+} concentration. For x=1 sample, a band near 655 cm^{-1} corresponds to the bending and stretching vibrations of GaO_4. The translational motion of GaO_4 tetrahedron generates a band in the lower wavenumber region.[39, 41]

The FWHM of XRD patterns and Raman spectrum are demonstrated in Figure S3, which can prove the orderliness of samples. The x=1 sample shows a narrow FWHM (full width at half maximum) of Raman spectra, which demonstrates it owns an ordered structure. The DFT calculation results, NMR spectra, and Raman spectra show that the new introduced Ga^{3+} ions tend to occupy the tetrahedral sites, but the Li^{+} ion occupation is dependent on the content. The tetrahedral sites are occupied by Li^{+} ions at a low content with $x \leq 0.4$, and they partially enter octahedral sites at a higher content with x=0.6. When x reaches 1, Li ions completely occupy the octahedral sites. Increase of x value from 0 to 1 leads to crystal structure experience a process from order to disorder and back to order. (Figure 4c).

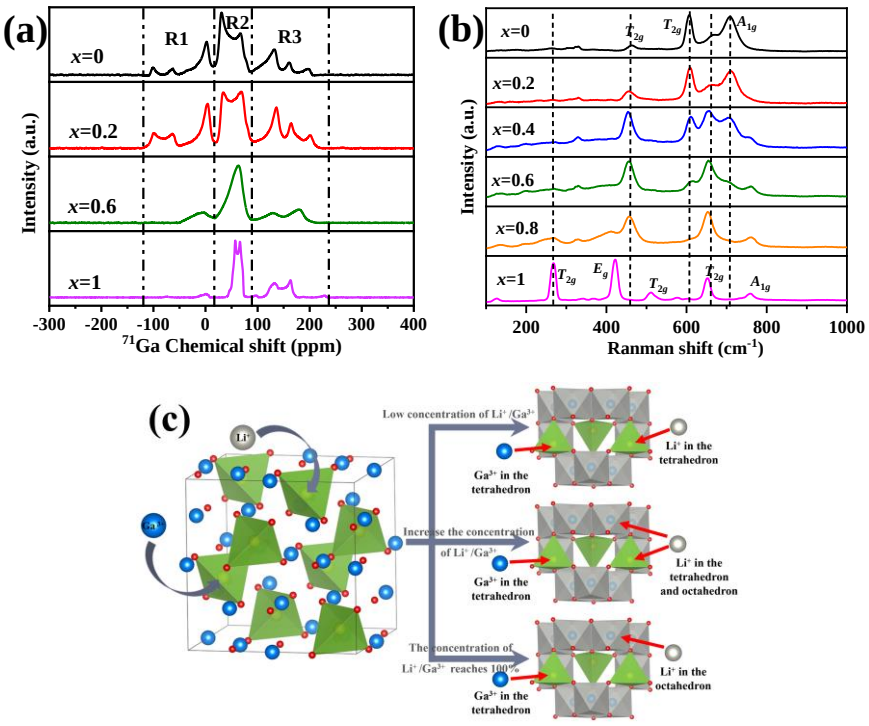

Figure 4. (a) ^{71}Ga MAS NMR spectra, (b)Raman spectra of ZLGGO, and (c) schematic illustration of Li^{+}/Ga^{3+} in tunable site occupations.

Table 2. The quantification of Ga^{IV}/Ga^{VI} proportion.

x	R1	R2	R3	Ga^{IV}/Ga^{VI}
0	6.09×10^{9}	1.36×10^{10}	6.52×10^{9}	3.2%
0.2	8.41×10^{9}	1.44×10^{10}	9.14×10^{9}	5.1%
0.6	3.17×10^{9}	1.57×10^{10}	6.48×10^{9}	21.1%
1	3.61×10^{8}	5.48×10^{9}	3.98×10^{9}	66.1%

Rietveld refinement of the XRD pattern was conducted for the $Zn_{1-x}(Li/Ga)_xGa_2O_4$

powders based on the above structural analysis to investigate the effect of Li^+/Ga^{3+} substitution on the crystal structure and phase composition of the spinel phase (Figure 5a-d). The consistency between diffraction peaks and standard data card suggests that these samples are pure phase and have a structure evolution. The low values of the residual factors (R_p, R_{wp}, and χ^2) of the samples suggest that the results are credible (Table S2-S6). Incorporation of Li^+-Ga^{3+} to replace Zn^{2+}-Zn^{2+} in $ZnGa_2O_4$ induces shrink of the unit cell due to the smaller ionic radii sum of the Li^+-Ga^{3+} pair than that of Zn^{2+}-Zn^{2+} pair in $ZnGa_2O_4$, further resulting in shift of the diffraction peaks to higher angle side (Figure 1). The cell volumes, lattice parameters a=b=c, as well as M-O average bond length (M=Li/Zn/Ga) of MO_4 tetrahedra and MO_6 octahedra for ZGO samples obtained from Rietveld refinement manifest an obvious linear decrease (Table S1 and Figure 5e), further implying the unit cell becomes smaller by substitution of Zn^{2+}-Zn^{2+} with the Li^+-Ga^{3+} pair. According to the above analysis, the crystal structure of the polyhedron is drawn in Figure 5f: the mismatched ionic radius caused by co-doping Li^+-Ga^{3+} leads to the tetrahedra and octahedral tilting, which could further influence the crystal field of Cr^{3+} in ZLGGC phosphors.[42, 43]

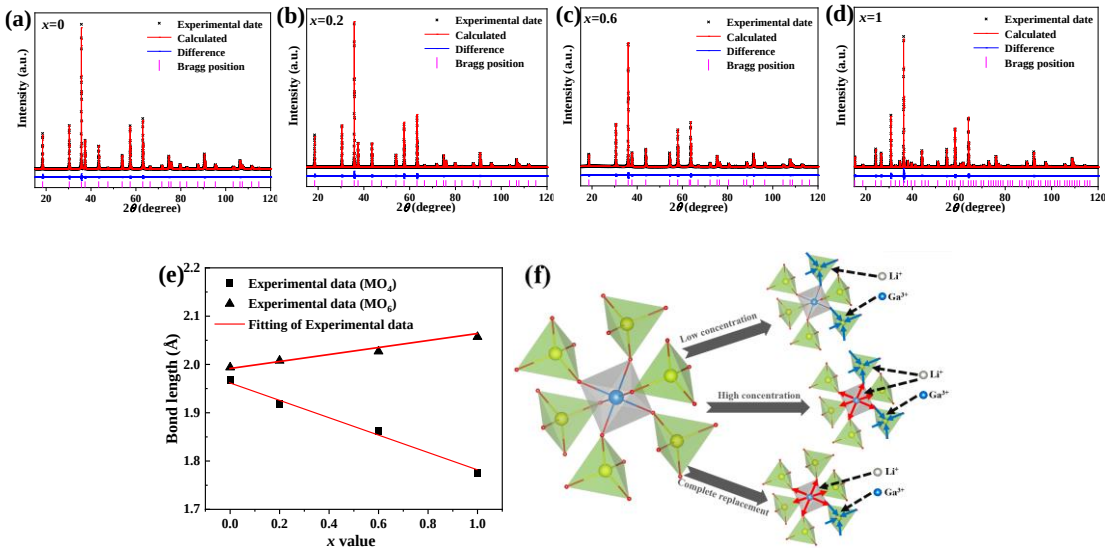

Figure 5. The results of Rietveld refinement for XRD patterns of ZLGGO host with different x values: (a) x=0, (b)x=0.2, (c)x=0.6, and (d) x=0.1, respectively. (e) is average bond length for MO_4 tetrahedron and MO_6 octahedron of ZLGGO (x=0-1). (f) is structural distortion trend with different doping contents.

The morphologies of ZLGGO samples obtained by TEM are shown in Figure S4a-d, which are irregular with dispersed micron and submicron particles, similar to those of high temperature solid-state reaction produced samples. The particle size is not affected by co-doping. High-resolution TEM (HR-TEM; Figure S4e-h) shows the clear lattice fringes spaces of 2.76, 2.67, 4.89, and 2.47 Å, which are assigned to the (220), (311), (111), and (311) planes for x=0, 0.2, 0.6 and 1 samples, respectively. Selected-area electron diffraction (SAED) exhibits a set of diffraction spots (Figure S4i-l), while the calculated d-spacings of 3.05, 3.02, 2.91 and 2.90 Å can be assigned to the (220) plane of cubic ZLGGO spinel. The results also indicate that the unit cell becomes smaller by substitution of Zn^{2+}-Zn^{2+} with the Li^{+}-Ga^{3+} pair.

3.2 Photoluminescence and persistent luminescence of ZLGGC

UV-vis reflection spectra can be used to measure the optical absorption bands of $Zn_{1-x}(Li/Ga)_xGa_2O_4$:0.005Cr^{3+} phosphors. In the diffuse reflection spectra (Figure 6a), all the samples show three common absorption broadbands, among which the band located at 200~320 nm corresponds to the $^4A_2 \rightarrow {}^4T_1$ (^4P) transition of Cr^{3+} and the band-gap transition (VB→CB), and the bands at ~410 and ~570 nm correspond to the $^4A_2 \rightarrow {}^4T_1$ (^4F) and $^4A_2 \rightarrow {}^4T_2$ (^4F) transitions of Cr^{3+}. [11, 22] It is noteworthy that the $^4A_2 \rightarrow {}^4T_2$ (^4F) transition of Cr^{3+} has an obvious redshift after Li^{+}/Ga^{3+} doping, illustrating that Li^{+}/Ga^{3+} doping gives rise to a weaker crystal field. The diffuse reflectance (R_∞) of ZLGGO was obtained (Figure S5) and converted by the Kubelka-Munk function, and it can be used to characterize the band structure in detail:[14, 30]

$$F(R_\infty) = (1- R_\infty)^2/2\, R_\infty \quad (3)$$

and the $[F(R_\infty)h\upsilon]^2$ verses $h\upsilon$ plots were obtained based on the following function:

$$[F(R_\infty)h\upsilon]^2 = A(h\upsilon - E_g) \quad (4)$$

where E_g and $h\upsilon$ are the bandgap energy and incident photon energy, respectively, and A is a constant. The $[F(R_\infty)h\upsilon]^2$- $h\upsilon$ plot of ZLGGO shown in Figure 6b was used to determine the bandgap energy, and from the intercept of a fitted straight line, the bandgap energy was determined to increase from 4.47 to 4.99 eV with increasing x value from 0 to 1 (Figure 6b).

The band structure was further evaluated by calculation of partial and total density

of states using density functional theory calculations for ZLGGO (Figure 6c-g). Results show that only the O orbital levels contribute to the valence band maximum, whereas both the O and Ga orbital levels contribute significantly to the conduction band minimum, consistent with previous reports.[22, 30] The calculated bandgap of perfect ZGO crystal (2.27 eV) is smaller than the experimental value (4.47 eV) (Figure 6c). Because the generalized gradient approximation (GGA) underestimates the bandgap size, all the calculated band structures using DFT approach are smaller than the experimental values (Figure 6c-l).[22, 25, 31] All the results from DFT calculations indicate that the bandgaps increase (from 2.274 to 2.482 eV) as the content of Li^{+}/Ga^{3+} increases (Figure 6c-l), which matches well with the local structure and the UV-vis analysis.

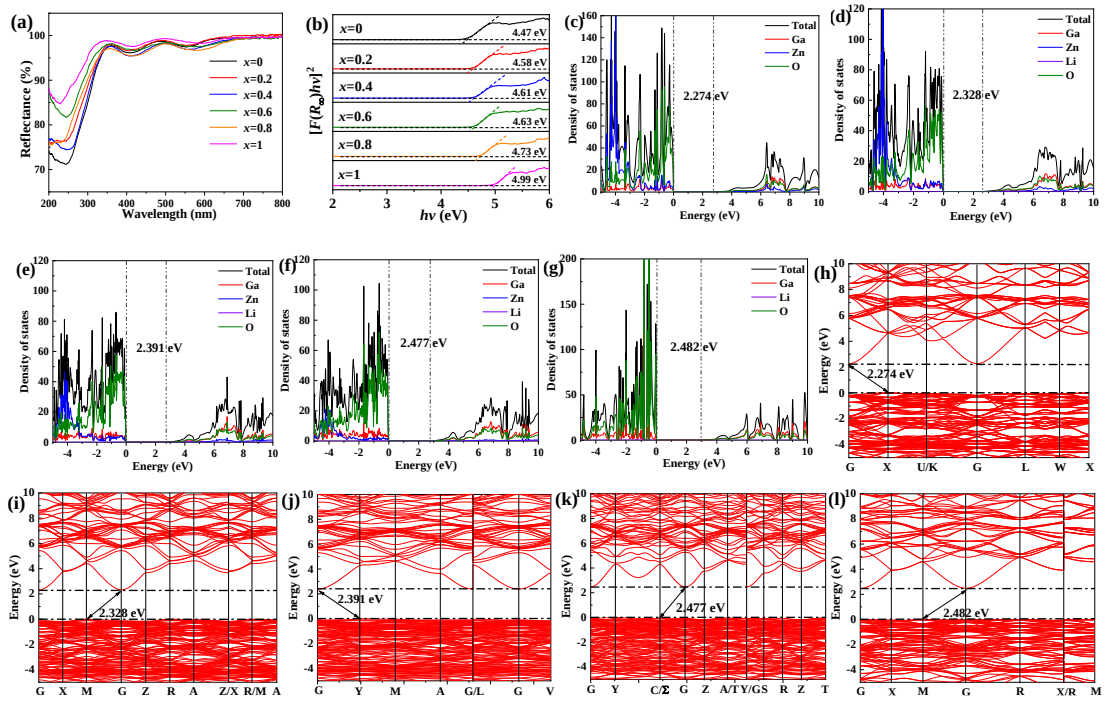

Figure 6. The band structures of ZLGGO: (a) UV-vis reflection spectra of ZLGGC, (b) $[F(R_\infty)h\upsilon]^2$- $h\upsilon$ plot of ZLGGO. (c-g) are total and partial density of states of ZLGGO: (c) 0%, (d) 25%, (e) 50%, (f) 75%, (g) 100%. The Fermi energy is taken as the zero of energy. (h-l) are the electronic band structure of ZLGGO: (h) 0%, (i) 25%, (j) 50%, (k) 75%, (l) 100%.

In chromium doped spinels, lattice disorder and perturbation arising from cation inversion and incorporation of new ions would give rise to the varied luminescence of

Cr^{3+}. The Cr^{3+} ion energy levels are sensitive to coordination and dependent on strength of crystal field with $3d^3$ electronic configuration.[3, 44, 45] Obtained by monitoring the Cr^{3+} emission peak at 708 nm, the photoluminescence excitation (PLE) spectra (Figure 7a and Figure S6a) demonstrate three strong bands corresponding to the band-gap transition (VB→CB) and the $^4A_2 \rightarrow {}^4T_1$ (^4P) transition with peak at ~260 nm (the strongest), the $^4A_2 \rightarrow {}^4T_1$ (^4F) transition with peak at ~409 nm, and the $^4A_2 \rightarrow {}^4T_2$ (^4F) transition with peak at ~554 nm. The PL spectra of the ZLGGC phosphors recorded at UV-light are shown in Figure 7b and Figure S6b. The intense emission bands at the wavelength range of 650-800 nm locate in the NIR area, which are assigned to the $^2E \rightarrow {}^4A_2$ transition of Cr^{3+}.[1-4, 10, 13] The sample Cr^{3+} luminescence is excited preferentially by UV range energies, in which the band-gap transition at about 250 nm corresponds to transition of electrons from oxygen orbitals to gallium orbitals (VB→CB) (Figure 7a).[14, 46] It can be found that with increasing Li^+/Ga^{3+} content, the excitation peaks of VB→CB shift to the short-wavelength side, consistent with band gap and band structure analysis. In the PLE spectra, the blue shift in the VB→CB is due to the enlarged *E*g for the Li^+/Ga^{3+} incorporated samples.[17, 47, 48] However, a different observation was found for the 3d-3d transitions of Cr^{3+}. The 3d-3d transitions shift to the long-wavelength side with increasing Li^+/Ga^{3+} content, which is correlated with the crystal field of host materials.[3, 45, 49] Under the 260 nm excitation, the samples output strong deep red and NIR emissions ($^2E \rightarrow {}^4A_2$ transition of Cr^{3+} at ~700 nm) as demonstrated in Figure 7b. For $ZnGa_2O_4$:0.005Cr^{3+}, the PL spectra display several narrow lines that indicates Cr^{3+} ion is in octahedral coordination with a strong field. Similar to the reported results, the emissions centered at 688 nm (~1.81 eV) are corresponded to the R1 and R2 zero phonon lines for the $^2E \rightarrow {}^4A_2$ transition of Cr^{3+}.[2, 50] As previously reported, N2-lines are dependent on the host lattice structure, and they arise from Cr^{3+} ions in distorted octahedron. In addition, all N-lines are spectroscopic analogs of R-line and can be interpreted as zero-phonon lines of different luminescence centers. In Figure 7b, the peak at ~695 nm corresponds to another type of Cr^{3+} ion with perturbed short-range crystalline order different from the ideal octahedral coordination of the normal spinel, and the peak at 708 nm (14124 cm^-

^{1}) has ~400 cm^{-1} lower energy than the R line, showing a strong emission.[2, 50] According to the report of Mikenda et al., in $ZnGa_2O_4$, the structure-dependent line N4 for Cr^{3+} lies at ~400 cm^{-1} lower energy than R1, so it is quite possible that the 708 nm line is attributed to the N4 line of Cr^{3+}. [51] Here, the N2 and N4 lines of Cr^{3+} in $ZnGa_2O_4$ spinel are originated from the Cr^{3+} ions in two kinds of distorted environments, which are around the antisite defects and the defects arising from Li occupying Zn site, respectively. The R lines peak at the range of 650-750 nm and are accompanied by their anti-Stokes (AS) and Stokes (S) Phonon Side Bands (PSB). The PSB of N2 and N4 lines, which also exists at 650-750 nm, presents broader while less intense features than PSB of R lines. Increasing Li^{+}/Ga^{3+} results in reduced intensities of zero phonon R lines and decreased vibrionic PSB, as well as red shift of emission peaks. When *x* reaches 1, the emission peak has obvious change: The emission peak centers at ~718 nm, corresponding to the Cr^{3+} zero-phonon emission from ^{2}E to $^{4}A_2$ level. The emission band at 650~750 nm corresponds to the $^{4}T_2 \rightarrow {}^{4}A_2$ transition, which contains both the anti-Stokes and Stokes PSB.

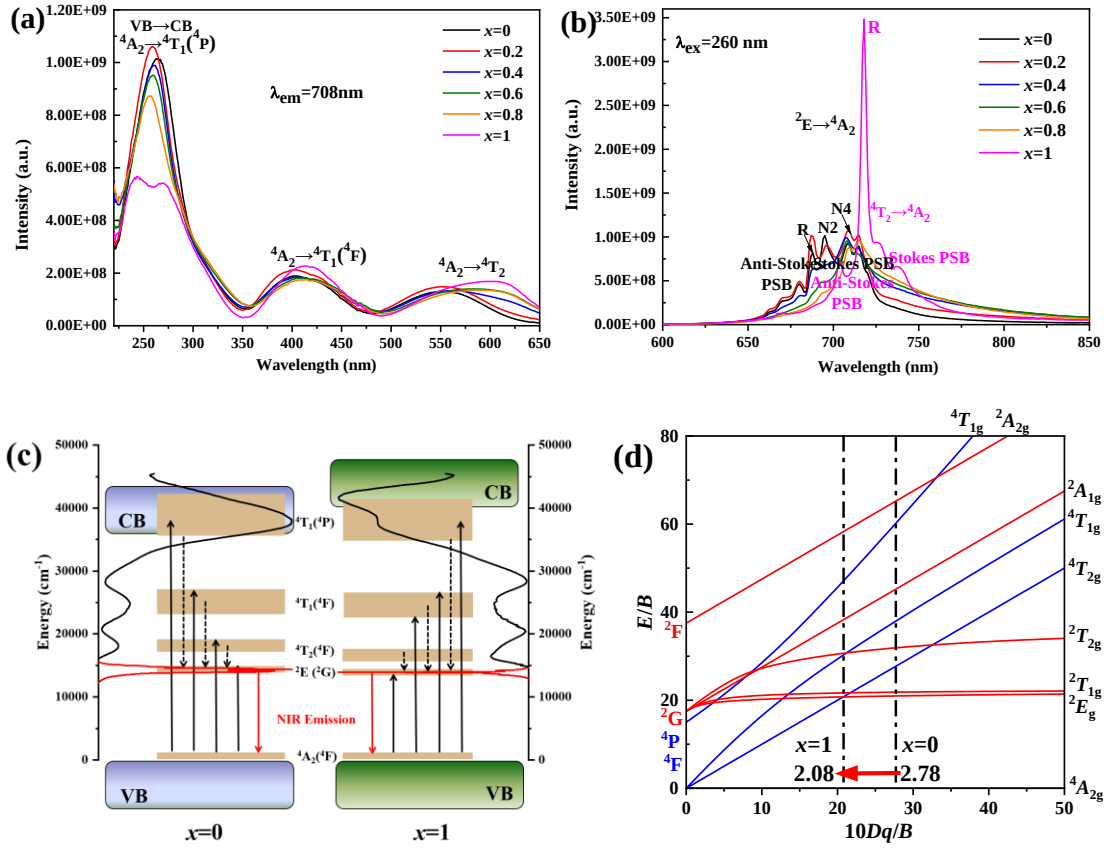

Figure 7. (a) PLE and (b) PL spectra of ZLGGC at room temperature. (c) Mechanism

diagram of luminescence in ZLGGC phosphors. (d) Tanabe-Sugano energy-level diagram of Cr^{3+} in x=0 and x=1 samples.

According to the reports, the Racah parameters B and C were estimated for mean peak energies of $^4A_2 \rightarrow {}^4T_2$ and $^4A_2 \rightarrow {}^4T_1$ bands, and the crystal field strength was evaluated using the crystal field parameter (Dq) from the mean peak energy of the $^4A_2 \rightarrow {}^4T_2$ transition, based on the PLE data at room temperature:[3, 44-46, 52]

$$10D_q = E(^4T_2) - E(^4A_2) \quad (5)$$

$$Dq/B = 15(x-8)/(x^2-10x) \quad (6)$$

$$x = [E(^4T_2) - E(^4A_2)]/Dq \quad (7)$$

$$C \cong E(^4T_2) - E(^4A_2) \quad (8)$$

and the calculated values are listed in Table 3. The estimated values of B=652.8 cm^{-1}, Dq=1818.2 cm^{-1}, and Dq/B=2.78 for x=0 sample clearly agree with the existed reports showing that by following the calculated energy level diagram for Cr^{3+} in octahedral symmetry, the Cr^{3+} embedded in the zinc gallate host is subject to a strong crystal field approximation. [45] Meanwhile, the ratios of Dq/B are determined to be 2.77 (x=0.2), 2.57 (x=0.4), 2.29 (x=0.6), 2.20 (x=0.8) and 2.08 (x=1), which indicate that crystal field strength decreases as Li^+/Ga^{3+} doping content increases. It can be seen that the energy levels of $^4T_1$ and $^4T_2$ are closely correlated with the crystal field strength. The energy gap between the ground state ($^4A_2$) and the excitation state ($^4T_1$ and $^4T_2$) can be narrowed by weaker crystal field strength, leading to red shift of the 3d Cr^{3+} transitions. It is worth considering that the crystal field strength is closely correlated with the parameters affecting outer orbits. To figure out the real reasons, a deeper understanding of the parameters that affect outer orbits is needed. Brik et al. introduced a new parameter of the nephelauxetic effect β as follows to explore the relationship between the covalence of the metal-ligand chemical bonds and the energies of the lowest energy spin-forbidden transition $^2E_g \rightarrow {}^4A_{2g}$:[44, 53]

$$\beta = [(B/B_0)^2 + (C/C_0)^2]^{1/2} \quad (9)$$

where B_0, C_0 (C_0 = 3850 cm^{-1} and B_0 = 918 cm^{-1}) and B, C are the Racah parameters of Cr^{3+} in free and crystal states, respectively. β increases from 1.09 to 1.12 with the increasing x from 0 to 1, indicating an increased bonding of Cr^{3+}-ligand.

The peak of $^2E \rightarrow {}^4A_2$ transition in emission spectra only shows a slight red shift compared to the large shift observed in excitation spectra since the energy gap between the ground state and the ^2E level is insensitive to the changes of crystal field strength.[54] The PLE/PL spectra of ZLGGC at low temperature demonstrate the similar pattern as shown in Figure S7. Figure 7c shows the mechanism diagram of luminescence for ZLGGC phosphors based on the above results. The electrons of Cr^{3+} in ZLGGC are pumped from $^4A_2$ (ground state level) to $^4T_2$ (^4F), $^4T_1$ (^4F), $^4T_1$ (^4P) (excited state levels), and conduct band, then transferred to ^2E and $^4T_2$ level through non-radiative relaxation, and eventually changed to $^4A_2$ state, which has a good NIR light output. With increasing value of *x*, the PLE and PL spectra exhibit distinct redshift. This phenomenon can be explained utilizing Tanabe-Sugano energy-level diagram in Figure 7d.

Table 3. Energy states, crystal field parameters and calculated values of ZLGGC.

Simple	$^4A_2$-$^4T_1$(cm^{-1})	$^4A_2$-$^4T_2$(cm^{-1})	$^4A_2$-^2E(cm^{-1})	*Dq*	*Dq*/*B*	*B*	*C*	*β*
x=0	24875	18182	14388	1818	2.78	652.8	3163.4	1.09
x=0.2	24814	18116	14144	1812	2.77	654.1	3081.2	1.07
x=0.4	24752	17794	14144	1779	2.57	690.8	3004.9	1.08
x=0.6	24450	17153	14124	1715	2.29	746.2	2887.7	1.10
x=0.8	24331	16920	13986	1692	2.20	767.0	2802.0	1.11
x=1	24155	16584	13926	1658	2.08	798.7	2721.9	1.12

3.4 Trap energy up-conversion-like NIR persistent luminescence in Bioimaging

Figure S8a shows the afterglow decay curves of ZLGGC phosphors monitored at 695-718 nm after an irradiation using 254 nm UV light for 10 min. The results showed that in the first 500 s, the afterglow intensity of all phosphors rapidly drops, followed by a slow decrease, which is correlated with the release speed of electrons from the traps. Afterglow decay curves and time-dependent afterglows of ZLGGC phosphors (Figure S8a and 8a) demonstrate similar phenomenon that with increasing value of *x* from 0 to 0.8, the afterglow intensity increases, but further increase of the Li^+/Ga^{3+} content ($x > 0.8$), it drops. Figure S8b shows the persistent luminescence

spectra with x = 0.8 phosphor as an example. It is shown that the spectra own a band with the peak at ~708 nm, indicating that the phosphors outputs excellent NIR afterglow, which can last more than 2 h. The TL curve of ZLGGC samples was measured at the temperature of 300-450 K to explore the trap depth and distribution (Figure 8b, Figure S9). The trap density n and trap depth E are estimated according to the equations: [22, 55, 56]

$$E = T_m/500 \quad (10)$$

$$n = \omega I_m/\{\beta\times[2.52+10.2\times(\mu_g-0.42)]\} \quad (11)$$

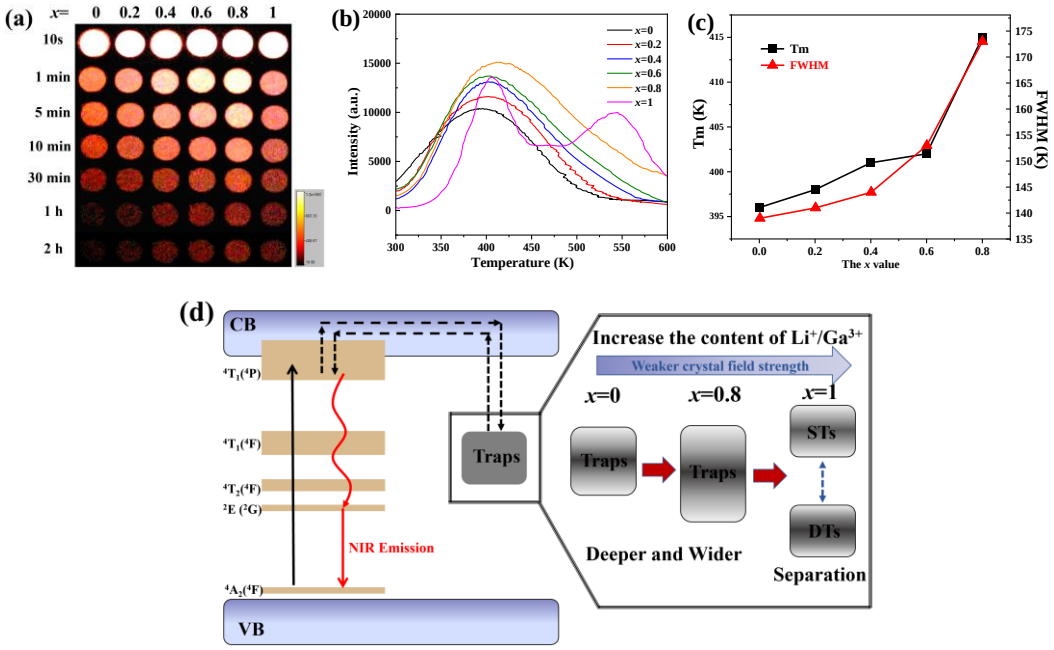

Figure 8. (a) Time-dependent NIR afterglows of ZLGGC after 254 nm UV light illumination for 10 min. (b) TL curves of ZLGGC after 254 nm UV light illumination for 10 min. (c) Tm and FWHM of the TL bands for different x values. (d) Schematics illustrating the multi-trap energy level diagram with the x increasing.

All statistics are demonstrated in Table S7. The x=0.8 sample outputs the best persistent luminescence because it has the deepest trap depth and the highest electron trap density. It is known that most of the TL bands have asymmetric shapes. The trap energy is assumed to have a "quasi-continuous" distribution, in which case a well-defined TL peak is not observed, but a broad peak composed of several closely spaced TL peaks superimposed. In this study, with the increase of x value (higher Li^+/Ga^{3+} content), the TL peaks gradually moved to high temperature, the full-width at half

maximum (FWHM) gradually increased and split into two peaks when x=1 (Figure 8b). It's fantastic that two broad bands appear in the TL curve of the x=1 sample, and the centers are at 405 K and 544 K, respectively, which indicates that the x=1 sample owns two kinds of traps, including deep traps (DTs) and shallow traps (STs). Figure 8c additionally shows the FWHM of the TL band and the peak temperatures of the TL bands (Tm), as a function of the x value. It is seen that the FWHM and peak temperatures of the TL bands are 139/396, 141/398, 144/401, 153/402 and 173/415 K for x=0, 0.2, 0.4, 0.6 and 0.8, respectively. This phenomenon is closely related to the crystal structure and crystal field strength: it may be that the increase of Li^+/Ga^{3+} content leads to the decrease of crystal field, which further deepens the trap depth and widens the energy level, similar to the centroid shift of Ce^{3+} ion luminescence, which has also been observed in previous studies.[22, 57] The multi-trap energy level diagram (Figure 8d) was drawn according to Figure 8b and 8c: with the increase of the x value, there are two effects :(1) the trap energy level center moved down; (2) the trap energy level coverage area gradually increased. When $x \leq 0.8$, there are many lattice defects in the sample, which are in disordered state. The crystal field strength is greater than 2.10, thus Cr^{3+} ions are in strong crystal field with $^2E \rightarrow {}^4A_2$ transition dominating, which causes continuously distributed trap energy level gradually moves down and becomes wider. When x reaches 1, the crystal field strength is less than 2.10. Therefore, Cr^{3+} ions are in weak crystal field, which causes the trap level splitting into two divided traps including deep traps (DTs) and shallow traps (STs). This further makes the deep trap energy level and ^2E energy level are prone to electron transfer by tunneling. The splitting of two kinds of traps in x=1 sample means that the rate of electron transfer between DTs and STs may decrease, which favors the DTs to preserve the charged electrons and sets the stage for the subsequent prolonged the low-energy-excitation afterglow.[26, 55, 56, 58]

To further explore the spatial distributions of trap energy levels following optical excitation, TL spectra of the x=1 sample were detected at 0 min, 30 min, and 24 h after ceasing the UV excitation (Figure 9a, Figure S10). The low-temperature TL band shifts from 405 to 476 K when the interval time following UV irradiation increases

from 0 s to 30 min and 24 h, while little change was observed in the high-temperature band intensity peaked at 544 K, indicative of carrier exhaustion in STs and little release of the carriers in DTs. These results suggest that the trapping process consists of two steps, the shallow trapping step and DTs capture step (Figure 9b): first, following pumping of high-energy photon, the charge carriers are introduced into shallow traps; second, the carriers are further filled into deeper traps via nonradiative relaxation. In addition to the conventional capture of carriers from STs to DTs, the mechanism also involves an up-conversion-like electron transition from DTs to STs. Based on previous reports, ZGC has a NIR persistent luminescence repeatedly activated by red light (~650 nm). NIR excitation (Longer-wavelength) maybe more beneficial for bioimaging because it can reduce tissue scattering, thereby increasing effective in vivo penetration depth.[26] To investigate the existence of electron transition from DTs to STs in the system, ~650 nm red (25 W) and ~740 nm NIR LED (25 W) were used to estimate the ability to re-excitation. Time-dependent afterglows and afterglow decay curves of ZLGGC phosphors were demonstrated in Figure S11 and S12. The results indicate that samples own a better afterglow after the ~650 nm red LED excitation (There's not much difference in intensity.) and the x=1 sample exhibits the best afterglow after low energy excitation, which is mainly due to that trap splitting reduces the rate of electron transfer from the deep trap to the shallow trap. However, under the same thickness of pork (5 mm), the x=1 sample particles demonstrate a better afterglow after the ~740 nm NIR LED excitation than the ~650 nm red LED excitation since longer-wavelength NIR excitation can decrease tissue scattering (Figure S13). Therefore, a large irradiation area NIR LED (~740 nm) was utilized as light source in the subsequent tests (Figure S14). With a pork thickness of 2 cm, the x=1 sample particles covered by pork still maintained ~30% emission intensity compared to the x=1 sample particles not covered by pork under the 254 nm-UV light (Figure S15). After ceasing the ~740 nm NIR LED excitation, the afterglow decay curve in Figure S16 clearly shows that NIR irradiation leads to the afterglow at 718 nm lasting more than 1500 s.

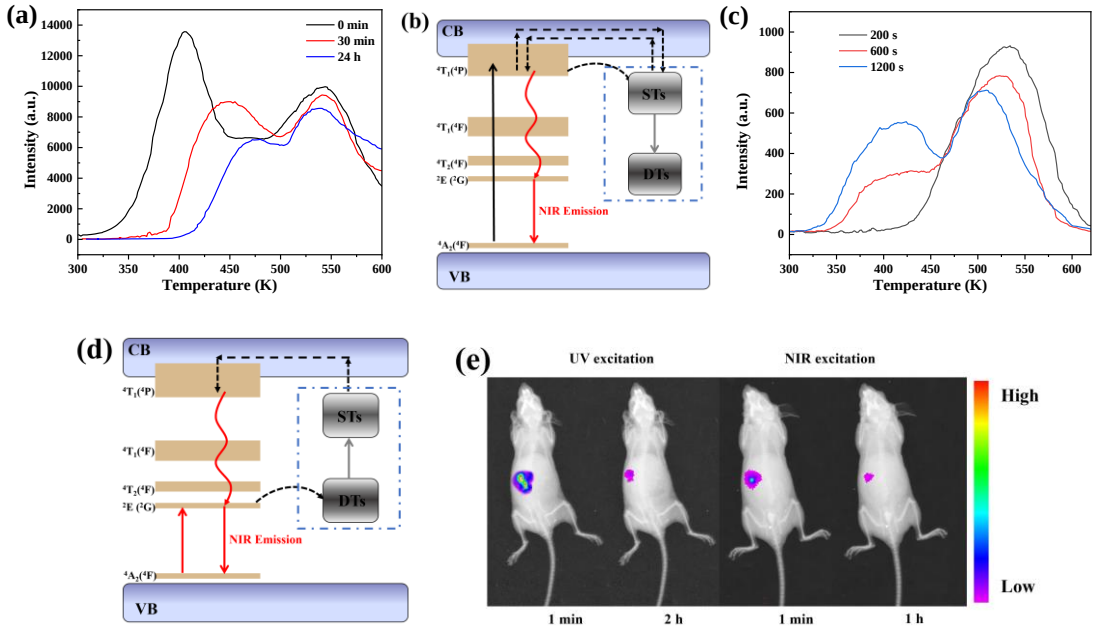

Figure 9. (a) TL spectra of *x*=1 sample after ceasing the UV excitation (excitation wavelength: 254 nm; exposure time: 10 min; interval time: 30 s, 30 min, and 24 h). (b) Schematics illustrating the normal trapping mode of deep traps (DTs). (c) TL curves of *x*=1 sample were measured using the ~740 nm NIR LED (25 W) with different excitation times (exposure time: 200, 600, and 1200 s). (d) Schematics illustrating the up-conversion trapping process from DTs to STs under the low energy excitation. (e) *In vivo* NIR afterglow images of a nude mouse (BALB/cA-nu adult mouse) after intramuscular injection of LGC-NH_2 solution (1 mL, 2 mg·mL^{-1}, 10 min exposure to a 254 nm UV light before injection) and recharging NIR afterglow decay images after 20 min secondary excitation with a ~740 NIR LED lamp.

To investigate the existence of electron transition from DTs to STs in this system, the TL curves of the *x*=1 sample were measured using the ~740 nm NIR LED as excitation source with different excitation times. After a 200-s irradiation with NIR LED (~740 nm), a distinct TL peak was observed at 530 K in the TL spectra (Figure 9c, Figure S17). With time increasing from 200 to 1200 s, the TL peak shifted from 540 to 507 K, and a new low-temperature TL peak was observed at 410 K, suggesting that the exposure time can affect the distribution of carriers in DTs and STs. Meanwhile, the afterglow has been extended with the exposure time changing from 200 to 1200 s, which further indicates the transfer of electrons from DTs to STs

(Figure S18). All the results imply that the trapping process and NIR excited persistent luminescence are as follows (Figure 9d): Under the NIR excitation, the electrons are pumped from ^2E to $^4A_2$, and the excited electrons are captured by the DTs through tunneling; under the NIR irradiation, some electrons are stored in the DTs and some are pumped into the STs like up-conversion energy transfer, which leads to the NIR emission; removing the NIR light source, the stored electrons release from DTs to STs and then to the excited energy level of Cr^{3+} ions, which finally contributes to the NIR afterglow. The energy storage based on the up-conversion-like trapping process also requires reproducibility and photostability under irradiation of NIR, which are essential for reliable biological imaging. [4, 5] Therefore, the attenuating spectra after four ~740 nm NIR LED irradiation are shown in Figure S19. The initial intensity and decay duration remained essentially unchanged even following more than eight on/off cycles (Figure S20). In order to realize the near infrared light renewable charging in biological imaging, the nanoparticles of x=1 sample with good dispersion and size within 200 nm were collected by sieving (Figure S21). Before the *in vivo* imaging experiment, the Cell Counting Kit-8 assay was performed on RAW264, A549-1, and HEK293T cells to assess the cytotoxicity of LGC-NH_2 (Figure S22), which confirms the low toxicity of LGC-NH_2 to the cells. The nanoparticles-NH_2 glucose solution (1 mg·mL^{-1}) was exposure to the 254-nm UV light for 10 minutes for *in vivo* imaging. After irradiation process, 500 μL of the irradiated aqueous solution was injected subcutaneously into a nude adult mouse on the belly and the NIR afterglow signal was tested for bioimaging analysis. [16, 59] The intense signal of NIR afterglow could be detected during the test time throughout the mouse body with no further excitation treatment, although signal loss took place over time. The afterglow luminescence signal lasted for at least 2 h (Figure 9e) under such NIR excitation. To assess the repeatability under such NIR excitation, the nude adult mice were subjected to a 20-min *in situ* excitation using NIR LED lamp (~740 nm). Following red-light excitation, repeatable NIR afterglow signal appeared, which could last for more than 1 h (Figure 9e). The above results suggest that the prepared Cr^{3+}-doped gallate probes are the effective fluorescent dyes for NIR light recovery

afterglow to enhance bioimaging by connecting the electron transport channel from DTs to STs.

4. Conclusion

In this study, a series of $Zn_{1-x}(Li/Ga)_xGa_2O_4:Cr^{3+}$ (x=0-1) NIR persistent luminescent phosphors were synthesized using a solid-state reaction. The characterization of the samples was achieved by Raman, DFT calculations, XRD, UV-Vis-NIR, NMR, Rietveld refinement, TL, PLE/PL spectroscopy, and persistent luminescence decay analysis. With the increase of Li^+/Ga^{3+} content in $ZnGa_2O_4$, all the newly introduced Ga^{3+} ions occupy the tetrahedral sites, but Li^+ ions firstly occupy the tetrahedral sites, then partially enter the octahedral sites, and completely occupy the octahedral sites when x reaches 1. These contribute to the contraction of tetrahedron and the expansion of octahedron, as well as changing the structure from order to disorder and back to order. Incorporation of Li^+/Ga^{3+} results in the decrease of lattice constant and the increase of band gap. The crystal field strength of phosphors decreases as Li^+/Ga^{3+} content increases, which makes a redshift of the emission and excitation spectra. The crystal field also affects the trap depth and distribution. When the crystal field becomes weaker, the trap depth becomes deeper and the trap energy level becomes wider and tends to splitting into two-divided energy levels. This makes deep trap energy level be near to the ^2E energy level of Cr^{3+}. A complete replacement of Zn^{2+} by Li^+/Ga^{3+} ions leads to the splitting of the trap energy level, which reduces the electron transfer between DTs and STs, but enhances the NIR afterglow of the samples, which are excited by the low-energy NIR light. This work provides a new category for the NIR-absorptive-NIR-emissive phosphors and a new application for long-term biological imaging.

Author Contributions

Qi Zhu and Ji-Guang Li conceived the project; Junqing Xiahou, Minghui Jin, and Fan Li carried out the experiments; Junqing Xiahou carried out the data analysis; Lin Zhu

carried out the DFT calculations; Qi Zhu and Junqing Xiahou drafted the manuscript and performed the analysis. All the authors were involved in the results discussion, and have read and approved the final manuscript.

Conflicts of interest

The authors declare that they have no conflict of interest.

Acknowledgments

This work was supported in part by the Natural Science Foundation of Liaoning Province (Grant 2020-MS-081), and National Natural Science Foundation of China (Grants 51302032, U21A2045, 52172112).

References

1. Z. Pan, Y. Y. Lu and F. Liu, Sunlight-Activated Long-Persistent Luminescence in the Near-Infrared from Cr^{3+}-Doped Zinc Gallogermanates, *Nat. Mater.*, 2011, **11**, 58-63.
2. A. Bessière, S. K. Sharma, N. Basavaraju, K. R. Priolkar, L. Binet, B. Viana, A. J. J. Bos, T. Maldiney, C. Richard, D. Scherman and D. Gourier, Storage of Visible Light for Long-Lasting Phosphorescence in Chromium-Doped Zinc Gallate, *Chem. Mater.*, 2014, **26**, 1365-1373.
3. L. Huang, L. Lin, W. Xie, Z. Qiu, H. Ni, H. Liang, Q. Tang, L. Cao, J.-X. Meng and F. Li, Near-Infrared Persistent Luminescence in a Cr^{3+}-Doped Perovskite for Low-Irradiance Imaging, *Chem. Mater.*, 2020, **32**, 5579-5588.

4. T. Maldiney, A. Bessiere, J. Seguin, E. Teston, S. K. Sharma, B. Viana, A. J. Bos, P. Dorenbos, M. Bessodes, D. Gourier, D. Scherman and C. Richard, The in Vivo Activation of Persistent Nanophosphors for Optical Imaging of Vascularization, Tumours and Grafted Cells, *Nat. Mater.*, 2014, **13**, 418-426.

5. J. Shi, X. Sun, J. Li, H. Man, J. Shen, Y. Yu and H. Zhang, Multifunctional Near Infrared-Emitting Long-Persistence Luminescent Nanoprobes for Drug Delivery and Targeted Tumor Imaging, *Biomaterials*, 2015, **37**, 260-270.

6. F. Liu, W. Yan, Y. J. Chuang, Z. Zhen, J. Xie and Z. Pan, Photostimulated Near-Infrared Persistent Luminescence as a New Optical Read-Out from Cr^{3+}-Doped $LiGa_5O_8$, *Sci. Rep.*, 2013, **3**, 1554.

7. Y. Lv, D. Ding, Y. Zhuang, Y. Feng, J. Shi, H. Zhang, T. L. Zhou, H. Chen and R. J. Xie, Chromium-Doped Zinc Gallogermanate@Zeolitic Imidazolate Framework-8: A Multifunctional Nanoplatform for Rechargeable In Vivo Persistent Luminescence Imaging and pH-Responsive Drug Release, *ACS Appl. Mater. Interfaces*, 2019, **11**, 1907-1916.

8. Z. Li, Y. Zhang, X. Wu, L. Huang, D. Li, W. Fan and G. Han, Direct Aqueous-Phase Synthesis of Sub-10 nm "Luminous Pearls" with Enhanced in Vivo Renewable Near-Infrared Persistent Luminescence, *J. Am. Chem. Soc.*, 2015, **137**, 5304-5307.

9. J. Shi, X. Sun, S. Zheng, J. Li, X. Fu and H. Zhang, A New Near-Infrared Persistent Luminescence Nanoparticle as a Multifunctional Nanoplatform for Multimodal Imaging and Cancer Therapy, *Biomaterials*, 2018, **152**, 15-23.

10. M. Allix, S. Chenu, E. Véron, T. Poumeyrol, E. A. Kouadri-Boudjelthia, S. Alahraché, F. Porcher, D. Massiot and F. Fayon, Considerable Improvement of Long-Persistent Luminescence in Germanium and Tin Substituted $ZnGa_2O_4$, *Chem. Mater.*, 2013, **25**, 1600-1606.

11. Q. Zhu, J. Xiahou, X. Li, X. Sun and J.-G. Li, Defect Cluster Engineering in $ZnGa_{2-x}(Mg/Ge)_xO_4:Cr^{3+}$ Nanoparticles for Remarkably Improved NIR Persistent Luminescence, *J. Am. Ceram. Soc.*, 2021, **104**, 4594-4605.

12. B. Zhao, Q. Zhu, X. Sun and J.-G. Li, Co-Doping Zn^{2+}/Sn^{4+} in $ZnGa_2O_4:Cr^{3+}$ for Dynamic Near-Infrared Luminescence and Advanced Anti-Counterfeiting, *Ceram. Int.*, 2021, **47**, 17000-17007.

13. A. Abdukayum, J. T. Chen, Q. Zhao and X. P. Yan, Functional Near Infrared-Emitting Cr^{3+}/Pr^{3+} Co-Doped Zinc Gallogermanate Persistent Luminescent Nanoparticles with Superlong Afterglow for In Vivo Targeted Bioimaging, *J. Am. Chem. Soc.*, 2013, **135**, 14125-14133.

14. Y. Zhuang, J. Ueda and S. Tanabe, Tunable Trap Depth in $Zn(Ga_{1-x}Al_x)_2O_4$:Cr,Bi Red Persistent Phosphors: Considerations of High-Temperature Persistent Luminescence and Photostimulated Persistent Luminescence, *J. Mater. Chem. C*, 2013, **1**, 7849.

15. R. Zou, S. Gong, J. Shi, J. Jiao, K.-L. Wong, H. Zhang, J. Wang and Q. Su, Magnetic-NIR Persistent Luminescent Dual-Modal ZGOCS@MSNs@Gd_2O_3 Core-Shell Nanoprobes For In Vivo Imaging, *Chem. Mater.*, 2017, **29**, 3938-3946.

16. R. Zou, J. Huang, J. Shi, L. Huang, X. Zhang, K.-L. Wong, H. Zhang, D. Jin, J. Wang and Q. Su, Silica Shell-Assisted Synthetic Route for Mono-Disperse Persistent Nanophosphors with Enhanced In Vivo Recharged Near-Infrared Persistent Luminescence, *Nano Res.*, 2017, **10**, 2070-2082.

17. O. Q. De Clercq, L. I. D. J. Martin, K. Korthout, J. Kusakovskij, H. Vrielinck and D. Poelman, Probing the Local Structure of the Near-Iinfrared Emitting Persistent Phosphor $LiGa_5O_8:Cr^{3+}$, *J. Mater. Chem. C*, 2017, **5**, 10861-10868.

18. M. S. Relvas, M. R. N. Soares, S. O. Pereira, A. V. Girão, F. M. Costa and T. Monteiro, Trends in Cr^{3+} Red Emissions from $ZnGa_2O_4$ Nanostructures Produced by Pulsed Laser Ablation in a Liquid Medium, *J. Phys. Chem. Solids*, 2019, **129**, 413-423.

19. Y. Li, Y. Li, R. Chen, K. Sharafudeen, S. Zhou, M. Gecevicius, H. Wang, G. Dong, Y. Wu, X. Qin and J. Qiu, Tailoring of the Trap Distribution and Crystal Field in Cr^{3+}-Doped Non-Gallate Phosphors with Near-Infrared Long-Persistence Phosphorescence, *NPG Asia Mater.*, 2015, **7**, e180-e180.

20. Y. Zhuang, J. Ueda, S. Tanabe and P. Dorenbos, Band-Gap Variation and a Self-Redox Effect Induced by Compositional Deviation in $Zn_xGa_2O_{3+x}:Cr^{3+}$ Persistent Phosphors, *J. Mater. Chem. C*, 2014, **2**, 5502.

21. Y. Li, X. Du, K. Sharafudeen, C. Liao and J. Qiu, A Long Persistent Phosphor Based on Recombination Centers Originating from Zn Imperfections, *Spectrochim. Acta. A. Mol. Biomol. Spectrosc.*, 2014, **123**, 7-11.

22. J. Xiahou, Q. Zhu, L. Zhu, S. Li and J.-G. Li, Local Structure Regulation in

Near-Infrared Persistent Phosphor of $ZnGa_2O_4:Cr^{3+}$ to Fabricate Natural-Light Rechargeable Optical Thermometer, *ACS Appl. Electron. Mater.*, 2021, **3**, 3789-3803.

23. H. Guo, Y. Wang, W. Chen, W. Zeng, S. Han, G. Li and Y. Li, Controlling and rRevealing the Trap Distributions of $Ca_6BaP_4O_{17}:Eu^{2+},R^{3+}$ (R = Dy, Tb, Ce, Gd, Nd) by Codoping Different Trivalent Lanthanides, *J. Mater. Chem. C*, 2015, **3**, 11212-11218.

24. Y. Li, S. Zhou, Y. Li, K. Sharafudeen, Z. Ma, G. Dong, M. Peng and J. Qiu, Long Persistent and Photo-Stimulated Luminescence in Cr^{3+}-Doped Zn-Ga-Sn-O Phosphors for Deep and Reproducible Tissue Imaging, *J. Mater. Chem. C*, 2014, **2**, 2657.

25. H. Guo, W. Chen, W. Zeng, G. Li, Y. Wang, Y. Li, Y. Li and X. Ding, Structure and Luminescence Properties of a Novel Yellow Super Long-Lasting Phosphate Phosphor $Ca_6BaP_4O_{17}:Eu^{2+},Ho^{3+}$, *J. Mater. Chem. C*, 2015, **3**, 5844-5850.

26. X. Chen, Y. Li, K. Huang, L. Huang, X. Tian, H. Dong, R. Kang, Y. Hu, J. Nie, J. Qiu and G. Han, Trap Energy Upconversion-Like Near-Infrared to Near-Infrared Light Rejuvenateable Persistent Luminescence, *Adv. Mater.*, 2021, **33**, e2008722.

27. W. Lambrecht, Dopants and Defects in Semiconductors, *Materials Today*, 2012, **15**, 349.

28. P. Xiong, B. Huang, D. Peng, B. Viana, M. Peng and Z. Ma, Self-Recoverable

Mechanically Induced Instant Luminescence from Cr^{3+}-Doped $LiGa_5O_8$, *Adv. Funct. Mater.*, 2021, **31**, 2010685.

29. P. Xiong, M. Peng, K. Qin, F. Xu and X. Xu, Visible to Near-Infrared Persistent Luminescence and Mechanoluminescence from Pr^{3+}-Doped $LiGa_5O_8$ for Energy Storage and Bioimaging, *Adv. Opt. Mater.*, 2019, **7**, 1901107.

30. J. Xiahou, Q. Zhu, L. Zhu, S. Huang, T. Zhang, X. Sun and J.-G. Li, Lattice-Site Engineering in $ZnGa_2O_4$:Cr^{3+} Through Li^+ Doping for Dynamic Luminescence and Advanced Optical Anti-Counterfeiting, *J. Mater. Chem. C*, 2022, **10**, 7935-7948.

31. J. P. Perdew, K. Burke and M. Ernzerhof, Generalized Gradient Approximation Made Simple, *Phys. Rev. Lett.*, 1996, **77**, 3865.

32. L. Zhu, L. Li and T.-M. Cheng, First Principle Study of the Electrochemical Properties of Li_2FeSiS_4, *Comput. Mater. Sci.*, 2015, **106**, 135-139.

33. C. Bernuy-Lopez, W. Manalastas, J. M. Lopez del Amo, A. Aguadero, F. Aguesse and J. A. Kilner, Atmosphere Controlled Processing of Ga-Substituted Garnets for High Li-Ion Conductivity Ceramics, *Chem. Mater.*, 2014, **26**, 3610-3617.

34. L. Buannic, B. Orayech, J.-M. López Del Amo, J. Carrasco, N. A. Katcho, F. Aguesse, W. Manalastas, W. Zhang, J. Kilner and A. Llordés, Dual Substitution Strategy to Enhance Li^+ Ionic Conductivity in $Li_7La_3Zr_2O_{12}$ Solid Electrolyte, *Chem. Mater.*, 2017, **29**, 1769-1778.

35. D. S. Cook, J. E. Hooper, D. M. Dawson, J. M. Fisher, D. Thompsett, S. E. Ashbrook and R. I. Walton, Synthesis and Polymorphism of Mixed Aluminum-Gallium Oxides, *Inorg. Chem.*, 2020, **59**, 3805-3816.

36. S. Takahashi, A. Kan and H. Ogawa, Microwave Dielectric Properties of Spinel-Structured $Li_{0.5}Ga_{2.5}O_4$ Ceramics with Cation Ordering on Octahedral Sites, *Jpn. J. Appl. Phys.*, 2016, **55**, 10TE01.

37. D. Errandonea, ed., *Pressure-Induced Phase Transitions in AB_2X_4 Chalcogenide Compounds*, Springer, Berlin Heidelberg, 2014.

38. D. Li, Y. Wang, K. Xu, L. Li, Z. Hu and H. Zhao, Enhancement of Photoluminescence, Persistent Luminescence and Photocatalytic Activity in $ZnGa_2O_4$ Phosphors by Lithium Ion Doping, *Opt. Mater.*, 2015, **42**, 313-318.

39. P. Yadav, S. Uniyal, S. Uma and R. Nagarajan, Ordered $LiGa_5O_8$ Loaded with Redox Capable Cu^{2+}, Cr^{3+} Ions to Manifest Interesting Optical, Magnetic, and Catalytic Properties, *J. Mater. Sci.*, 2021, **56**, 20111-20125.

40. J. H. Park, B. W. Park, N. S. Choi, Y. T. Jeong, J. S. Kim and J. S. Yang, Enhancement in Cathodoluminescent Properties of Carbon Nanotube-$ZnGa_2O_4$:Mn^{2+} Phosphor Composites, *Electrochem. Solid-State Lett.*, 2008, **11**, J12-J14.

41. Y. Wang, J. Jiang, Z. Song and J. Zhang, Structural Characterization &, Optical and Electrical Properties of $LiGaO_2$ & $LiGa_5O_8$ Micro-Nanoparticles-Based Photodetectors, *J. Alloys Compd.*, 2021, **887**, 161438-161447.

42. N. Basavaraju, K. R. Priolkar, D. Gourier, A. Bessiere and B. Viana, Order and

Disorder around Cr^{3+} in Chromium Aoped Persistent Luminescent AB_2O_4 Spinels, *Phys. Chem. Chem. Phys.*, 2015, **17**, 10993-10999.

43. N. Basavaraju, K. R. Priolkar, D. Gourier, S. K. Sharma, A. Bessiere and B. Viana, The Importance of Inversion Disorder in the Visible Light Induced Persistent Luminescence in Cr^{3+} Doped AB_2O_4 (A = Zn or Mg and B = Ga or Al), *Phys. Chem. Chem. Phys.*, 2015, **17**, 1790-1799.

44. M. Back, E. Trave, J. Ueda and S. Tanabe, Ratiometric Optical Thermometer Based on Dual Near-Infrared Emission in Cr^{3+}-Doped Bismuth-Based Gallate Host, *Chem. Mater.*, 2016, **28**, 8347-8356.

45. Y. Tanabe and S. Sugano, On the Absorption Spectra of Complex Ions II, *J. Phys. Soc. Japan*, 1954, **9**, 766-779.

46. Q. Bai, S. Zhao, L. Guan, Z. Wang, P. Li and Z. Xu, Design and Control of the Luminescence of Cr^{3+}-Doped Phosphors in the Near-Infrared I Region by Fitting the Crystal Field, *Cryst. Growth Des.*, 2018, **18**, 3178-3186.

47. W. Huang, X. Gong, R. Cui, X. Li, L. Li, X. Wang and C. Deng, Enhanced Persistent Luminescence of $LiGa_5O_8:Cr^{3+}$ Near-Infrared Phosphors by Codoping Sn^{4+}, *J. Mater. Sci.: Mater. Electron.*, 2018, **29**, 10535-10541.

48. V. Singh, R. V. S. S. N. Ravikumar, G. Sivaramaiah, J. L. Rao and S. H. Kim, Investigations of the Optical and EPR Properties of $LiGa_5O_8:Cr^{3+}$ Phosphor, *Mater. Res. Bull.*, 2015, **61**, 183-188.

49. F. H. Teherani, D. C. Look, D. J. Rogers, S. K. Sharma, A. Bessiere, D. Gourier, G. Sraiki, B. Viana, P. J. Deren, D. Rudnicka, A. Watras, N.

Basavaraju, K. R. Priolkar, T. Maldiney, D. Scherman and C. Richard, Optical Poperties and Storage Capabilities in $AB_2O_4:Cr^{3+}$ (A=Zn, Mg, B=Ga, Al), *Proceedings of SPIE-The International Society for Optical Engineering*, 2014, **8987**, 89870J.

50. A. Bessière, S. Jacquart, K. Priolkar, A. Lecointre, B. Viana and D. Gourier, $ZnGa_2O_4:Cr^{3+}$: a New Red Long-Lasting Phosphor with High Brightness, *Opt. Express*, 2011, **19**, 10131-10137.

51. W. Mikenda, N-Lines in The Luminescence Spectra of Cr^{3+}-Doped Spinels (I): Identification of N-Lines *J. Lumin.*, 1981, **26**, 53-66.

52. T. Si, Q. Zhu, J. Xiahou, X. Sun and J.-G. Li, Regulating Mn^{2+}/Mn^{4+} Activators in $ZnGa_2O_4$ via Mg^{2+}/Ge^{4+} Doping to Generate Multimode Luminescence for Advanced Anti-Counterfeiting, *ACS Appl. Electron. Mater.*, 2021, **3**, 2005-2016.

53. M. G. Brik, S. J. Camardello, A. M. Srivastava, N. M. Avram and A. Suchocki, Spin-Forbidden Transitions in the Spectra of Transition Metal Ions and Nephelauxetic Effect, *ECS J. Solid State Sci. Technol.*, 2015, **5**, R3067-R3077.

54. S. Li, Q. Zhu, X. Sun and J.-G. Li, Magical Polyhedral Twist via Chemical Unit Co-Substitution in $LaAlO_3:Mn^{4+}$ to Greatly Enhance the Zero Phonon Line for High-Efficiency Plant-Growth LEDs, *J. Mater. Chem. C*, 2021, **9**, 7163-7173.

55. R. Chen, On the Calculation of Activation Energies and Frequency Factors from Glow Curves, *J. Appl. Phys.*, 1969, **40**, 570-585.

56. R. Chen, Glow Curves with General Order Kinetics, *J. Electrochem. Soc.*, 1969, **116**, 1254-1257.

57. Q. Meng, Q. Zhu, X. Li, X. Sun and J. G. Li, New Mg^{2+}/Ge^{4+}-Stabilized $Gd_3Mg_xGe_xAl_{5-2x}O_{12}$:Ce Garnet Phosphor with Orange-Yellow Emission for Warm-White LEDs (x = 2.0-2.5), *Inorg. Chem.*, 2021, **60**, 9773-9784.

58. Y. Li, M. Gecevicius and J. Qiu, Long Persistent Phosphors--from Fundamentals to Applications, *Chem. Soc. Rev.*, 2016, **45**, 2090-2136.

59. Q. Zhu, J. Xiahou, Y. Guo, H. Li, C. Ding, J. Wang, X. Li, X. Sun and J.-G. Li, $Zn_3Ga_2Ge_2O_{10}:Cr^{3+}$ Uniform Microspheres: Template-Free Synthesis, Tunable Bandgap/Trap Depth, and In Vivo Rechargeable Near-Infrared-Persistent Luminescence, *ACS Appl. Bio Mater.*, 2018, **2**, 577-587.